

JGR Space Physics



RESEARCH ARTICLE

10.1029/2025JA034171

Key Points:

- Modeled soft X-ray emission rates from Uranus's magnetosheath are up to ~ 10⁻¹⁰ photon cm⁻³ s⁻¹
- System geometry at equinox, rather than solstice, is preferential for generating soft X-rays in the magnetosheath
- Emission is strongly dependent on currently unconstrained moon-sourced neutral densities

Supporting Information:

Supporting Information may be found in the online version of this article.

Correspondence to:

D. Naylor, d.naylor@lancaster.ac.uk

Citation:

Naylor, D., Ray, L. C., Dunn, W. R., Jasinski, J. M., & Paty, C. (2025). Estimating soft X-ray emission from Uranus's magnetosheath. *Journal of Geophysical Research: Space Physics*, 130, e2025JA034171. https://doi.org/10.1029/2025JA034171

Received 6 MAY 2025 Accepted 9 NOV 2025

Author Contributions:

C. Paty

W. R. Dunn

Formal analysis: D. Naylor
Investigation: D. Naylor
Methodology: D. Naylor, L. C. Ray,
W. R. Dunn, C. Paty
Project administration: L. C. Ray
Resources: J. M. Jasinski
Software: D. Naylor, L. C. Ray,
W. R. Dunn
Supervision: L. C. Ray
Validation: D. Naylor
Visualization: D. Naylor
Writing – original draft: D. Naylor
Writing – review & editing: D. Naylor,
L. C. Ray, W. R. Dunn, J. M. Jasinski,

Conceptualization: D. Naylor, L. C. Ray,

© 2025. The Author(s).

This is an open access article under the terms of the Creative Commons

Attribution License, which permits use, distribution and reproduction in any medium, provided the original work is properly cited.

Estimating Soft X-Ray Emission From Uranus's Magnetosheath

D. Naylor¹, L. C. Ray¹, W. R. Dunn², J. M. Jasinski³, and C. Paty⁴

¹Space and Planetary Physics Group, Department of Physics, Lancaster University, Lancaster, UK, ²Department of Physics & Astronomy, University College London, London, UK, ³NASA Jet Propulsion Laboratory, California Institute of Technology, Pasadena, CA, USA, ⁴College of Arts and Sciences, University of Oregon, Eugene, OR, USA

Abstract Soft X-ray emission occurs within planetary magnetosheaths when highly charged solar wind ions undergo charge exchange with neutrals. The emission can provide dynamic views of the magnetosheath and cusps, allowing for investigations of the solar wind interaction with a planetary magnetosphere. The SMILE and LEXI missions will use soft X-ray imagers (SXIs) to explore the terrestrial magnetosheath. We explore the viability of a similar study at Uranus, where icy moons and the exosphere source neutrals. The neutrals undergo charge exchange with highly charged solar wind ions in the magnetosheath, causing soft X-ray emission. Here we present a simplified description of Uranus's magnetosheath to estimate emission rates. We estimate emission on the order of 10^{-10} photon cm⁻³ s⁻¹, corresponding to integration times for a SMILE-like SXI under 0.1 hr at $212 R_U$. Emission rates are higher at equinox than solstice. Emission rates are fairly constant for different solar wind conditions tested, apart from a low density sample where the emission is one order of magnitude lower. Testing the LEXI-like SXI under slow wind conditions gives integration times approximately double that of SMILE, ~5 minutes at 628 R_U . Improving the FOV and effective area of the SMILE SXI to test what a "future SXI" may look like reduces integration times to be ~3 s at $100 R_U$. Under a point source approximation, all SXIs perform well to ~10 au, with integration times remaining below 17 hr. Overall, this study supports further investigation of X-ray instrumentation possibilities for the Uranus flagship mission.

Plain Language Summary Soft X-rays are detected at different environments within the solar system. One example is a planetary magnetosheath. This is the region outside the magnetosphere containing slowed, heated solar wind, the continuous stream of plasma ejected from the Sun. Here, highly charged solar wind ions and neutral particles from the magnetosphere undergo charge exchange which results in soft X-ray emission. At Uranus, the exosphere and icy moons Miranda, Ariel, Umbriel, Titania and Oberon provide neutral particles. This model builds a simplified description of Uranus's complex magnetosphere to investigate the rates at which soft X-rays are emitted from the magnetosheath and the time it may take a soft X-ray imager (SXI) onboard an approaching spacecraft to image them. Integration times as low as 150 s are obtained when simulating a SMILE-like SXI on approach, but this can be further improved to be around 3 s by considering a future SXI with a larger field-of-view and effective area than SMILE. Finally, when considering the approach of an SXI to Uranus, X-rays can be imaged within a planetary rotation from distances as far as 10 au. Overall, this work supports further investigation of X-ray emission from the Uranian system.

1. Introduction

Uranus's magnetosphere is one of the most unusual environments in the solar system. With an axial tilt of 97.9° , Uranus orbits the Sun on its side, and its magnetic field is tilted 59° with respect to the rotation axis (Ness et al., 1986). The tilt and variation of the rotational geometry of the magnetosphere relative to the solar wind means the Uranian magnetosphere significantly varies over seasonal and diurnal timescales (e.g., Cao & Paty, 2017; Cao & Paty, 2021). Higher order quadrupole components are important to accurately model Uranus's magnetic field close to the planet (Ness et al., 1986), with the multipolar terms representable by an tilted dipole with an offset of $0.3~R_U$ (Paty et al., 2020). Overall, Uranus has a deeply complex, highly variable magnetosphere where the nature of the solar wind coupling is not well understood. This makes Uranus a prime candidate for the next NASA flagship-class planetary exploration mission, with a specific goal of understanding the link between the solar wind and the very complex magnetosphere (National Academies of Sciences, Engineering, and Medicine, 2023).

NAYLOR ET AL. 1 of 17



Uranus has only been visited once by NASA's Voyager 2 in 1986. This flyby provided information about the Uranian system during solstice (Stone & Miner, 1986). Analysis of plasma data by Richardson et al. (1990) looked at the conditions in the magnetosheath and found fluctuations in regions of rapidly varying magnetic field, suggesting a complex solar wind-bow shock interaction. Furthermore, recent reanalysis of the Voyager 2 data set by Jasinski et al. (2024) revealed that Voyager 2's flyby occurred at a time when the magnetosphere was in a very rare configuration (seen $\sim 4\%$ of the time), with the magnetosphere being both compressed and very likely plasma depleted. There have been efforts to model the magnetosphere of Uranus to fit with Voyager 2's results. These studies paint a picture of a complex magnetosphere with various interesting features (see Cao and Paty, 2014, 2021; Tóth et al., 2004). Notably, there is predicted to be a switch-like behavior where the open/closed configurations of the magnetosphere are driven by planetary rotation (Cao & Paty, 2017; Voigt et al., 1987).

Neutral particles exist within the Uranian magnetosphere, sourced from the icy moons Miranda, Ariel, Umbriel, Titania and Oberon. Neutrals are ejected from their parent body via sputtering processes as well as impact vaporization from the surfaces of the moons (Cheng, 1987; Eviatar & Richardson, 1986). H₂O dissociates and is predicted to form H, H₂, O, OH, H₂O and O₂ tori (Eviatar & Richardson, 1986). These neutral tori are confined to Uranus's equatorial plane, meaning at equinox, they are viewed edge-on from the Sun, while at solstice, they are viewed disk-on. The tori redistribute and diffuse throughout the system and models predict that there are neutral particles present at distances coincident with the magnetosheath (Cheng, 1987). However, neutral densities inferred from the Voyager flyby (Cheng, 1987) were lower than predicted ahead of arrival (Eviatar & Richardson, 1986). This discrepancy may be due to the compressed, likely plasma depleted state of the magnetosphere (Jasinski et al., 2024).

Soft X-ray emissions are ubiquitous across the solar system and often are found at planetary magnetosheaths, where shocked and slowed solar wind is deflected around the magnetopause (Connor et al., 2021; Snowden et al., 2004). They have been found at various environments in the solar system: Earth's magnetosheath (Carter & Sembay, 2008), comets (Cravens, 1997; Lisse et al., 1996), Jupiter's magnetosphere (e.g., Dunn et al., 2022), and the Moon (e.g., Collier et al., 2014). However, there have been no outer planetary missions with an objective of observing magnetosheath-sourced soft X-rays. In a magnetosheath, charge exchange occurs between O⁷⁺ and atomic hydrogen, where an electron is acquired from atomic hydrogen and transferred to the highly charged oxygen ion. This process partially neutralizes the ion and transfers the electron into an excited state. Upon deexcitation, soft X-rays (<2 keV) are emitted (Carter et al., 2010; Cravens et al., 2001; Snowden et al., 2004, see review by Dennerl (2008)). Modeling by Leppard et al. (2025) revealed that the soft X-ray signature from the Jovian magnetosheath is unlikely to be distinguishable from the background due to the vast system size and low neutral densities at the large distance the magnetosheath is located at, but there are several reasons why the case for Uranus may be more positive.

Imaging of soft X-rays is an emerging technology with several potential benefits. In the past, studies of the terrestrial magnetosheath and cusps have relied on in situ, local observations via spacecraft crossings. Soft X-ray imaging aims to better characterize the global, 3D structure of the regions as well as their dynamic responses to solar wind driving. Soft X-ray images can reveal a more global view of the location and shape of the magnetopause while continuous observations will give insights into how the large-scale boundary responds to variations in solar wind conditions, magnetic reconnection and magnetospheric current systems via the inference of magnetic field strengths just inside the magnetopause (Sibeck et al., 2018). They also aim to characterize more local, transient magnetosheath plasma phenomena such as high speed and density jets (Voitcu & Echim, 2024). Furthermore, soft X-ray imaging will allow for and characterization of the magnetospheric cusps and their response to solar wind and localization IMF changes (Sibeck et al., 2018). There are several examples of missions which use or have used soft X-ray imaging technology. One of these missions is SMILE, Solar wind Magnetosphere Ionosphere Link Explorer, a joint ESA and CAS venture due for launch in late 2025/2026, which will have a wide field-of-view (FOV) soft X-ray imager (SXI) on board with the aim of imaging Earth's magnetosheath in soft X-rays (Sembay et al., 2024). Another mission is LEXI, the Lunar Environment Heliophysics X-ray Imager, a NASA mission which landed on the Moon in January 2025 and similarly studied solar windmagnetosphere coupling through imaging soft X-rays from the lunar surface (Walsh et al., 2024). These missions build upon a large heritage of terrestrial solar wind charge exchange observations by multi-purpose X-ray observatories such as XMM-Newton (e.g., Carter & Sembay, 2008; Carter et al., 2011) and dedicating sounding

NAYLOR ET AL. 2 of 17



rockets (e.g., Galeazzi et al., 2011; Galeazzi et al., 2012; Thomas et al., 2013). This work aims to investigate whether soft X-ray imaging and its applications may be viable to employ on a Uranus orbiter mission.

This study uses simplified models of Uranus's magnetopause and bow shock to derive first estimations of soft X-ray emission rates generated within the magnetosheath, as well as the flux that could be detected by an SXI on approach to the system. Section 2 describes the model used in this study and presents baseline results. Section 3 reports the emission and flux changes for various neutral densities, solar wind conditions, and SXI configurations. Section 4 then presents our conclusions.

2. The Model

We approximate the Uranian system with a simple bullet-shaped magnetopause and bow shock. The tilt of the planet's magnetic axis is neglected, cusps are not present, and magnetosheath conditions are fixed. The tilt of the planet is simplified such that the equatorial plane of the planet is at 90° to its orbital motion, meaning in this model, the axial tilt of the planet is approximated to be 90° rather than $\sim 98^{\circ}$ as it is in reality. We estimate that this has negligible (>1%) effect on results, but simplifies the geometry considerably. The coordinate system used is such that the x-axis is oriented along the Uranus-Sun line, the y-axis is along the orbital plane of Uranus, and the z-axis completes the right-hand set.

2.1. Magnetopause and Bow Shock Surfaces

The magnetopause surface is based off that used by Cao and Paty (2021), who derived their work from the model of Shue et al. (1997), given by

$$r_{\rm MP} = r_0 \left(\frac{2}{1 + \cos \theta} \right)^K \tag{1}$$

where r_0 is the subsolar standoff distance in Uranus radii ($R_U = 25,559$ km), θ is the polar angle and K is the flaring parameter of the magnetopause.

Currently, there are no empirical models of the bow shock surface at Uranus, although Tóth et al. (2004) modeled the magnetosphere, including the bow shock, using MHD equations. For simplicity, the bow shock location (including flaring parameter) is approximated using Voyager 2 crossing data from Richardson et al. (1990) and the standoff location from the Tóth et al. (2004) model. These are combined with Equation 1 to provide the bow shock surface. The subsolar standoff distances, r_0 , used were $16\ R_U$ and $20\ R_U$ for the magnetopause and bow shock, respectively (Tóth et al., 2004). The flaring parameters, K, estimated from Figure 1 of Richardson et al. (1990), are 0.6 and 0.88 for the magnetopause and bow shock, respectively. The 3D structure of the surfaces is seen in Figure 1.

2.1.1. Solar Wind Conditions

The extent to which the solar wind drives Uranus's magnetosphere is unknown. However, it is suggested that there are fewer internal drivers than at the gas giants, meaning that the solar wind interaction potentially dominates magnetospheric dynamics at Uranus (Gershman & DiBraccio, 2024). Therefore, it is important to explore how the solar wind, which changes the shape, size and conditions of the magnetosheath, affects X-ray emission. Toth et al. (2004) imposed solar wind conditions based on, but not identical to, Voyager 2 data (Bridge et al., 1986). Their model uses $v_{SW} = 450 \text{ km s}^{-1}$, $n_{SW} = 0.1 \text{ cm}^{-3}$, $T_{SW} = 4.7 \text{ eV} = 54,541 \text{ K}$. This study imposes the same conditions, referred to henceforth as the default conditions, when solar wind variations are not being tested. In line with Toth et al. (2004), solar wind density is increased by a factor of four in the magnetosheath (see Prolss, 2010) to account for a strong shock, yielding a magnetosheath ion density of 0.4 cm⁻³. The other solar wind parameters are kept at their default values within the magnetosheath. Voyager 2 magnetosheath data, reported by Richardson et al. (1990), shows 0.4 cm⁻³ is at the higher range of detected ion density, but overall the modeled density is consistent with data.

In Section 3.2, samples of Voyager 2 solar wind data near Uranus's orbit (Jasinski et al., 2024) are imposed to test how solar wind variations affect X-ray emission rates. The magnetopause standoff distance is included in the data. The bow shock standoff distance is altered to reflect the change in magnetopause distance, with the ratio between

NAYLOR ET AL. 3 of 17

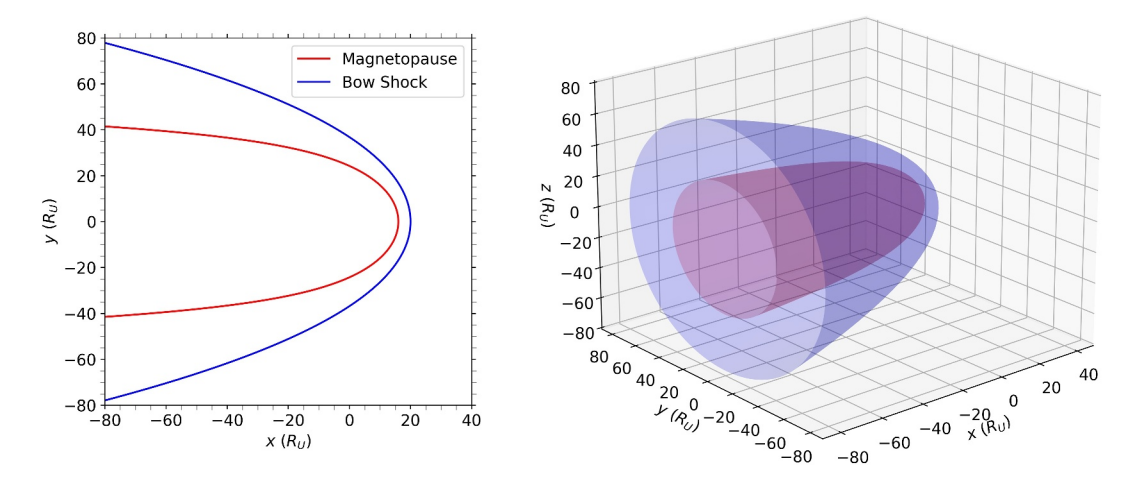


Figure 1. Bullet-shaped magnetopause (red) and bow shock (blue) surfaces, using the model of Shue et al. (1997). Here, $r_0 = 16 R_U$ (20 R_U) and K = 0.60 (0.88) for the magnetopause (bow shock). It is important to note that these surfaces are a significant simplification, with no treatment of the tilt of the magnetic axis from Uranus's spin axis, as well as the exclusion of the cusps. The left figure shows the surfaces in the x-y plane while the right figure shows the surfaces in 3D.

the two standoff distances fixed at 1.25 (Farris et al., 1991; Farris & Russell, 1994; Petrinec & Russell, 1997). The flaring parameters for the two surfaces are altered using 1/4 of the percentage difference between the original and new standoff distances.

Fast solar wind is also tested in Section 3.2. In this case, the magnetopause and bow shock standoff distance is estimated through use of the pressure balance equation, considering the change in standoff distances between fast and slow wind.

$$\frac{R_{\text{stand}}}{R_{IJ}} = \left(\frac{2B_{eq}^2}{\mu_0 m_p n_p v_{\text{GW}}^2}\right)^{\frac{1}{5.7}} \tag{2}$$

where R_{stand} is the standoff distance, B_{eq} is the equatorial field strength, μ_0 is the vacuum permeability, m_p is the proton mass, n_p is the proton density of the solar wind and v_{SW} is the solar wind speed. The 5.7 power has been fit to the Voyager 2 Uranus magnetopause crossing (Jasinski et al., 2024). All terms except the solar wind speed and density are taken to be constant for the simple comparison between slow and fast wind (fixed at the default conditions), therefore the difference between the standoff distances is calculated as

$$\frac{R_{\text{stand,slow}}}{R_{\text{stand,fast}}} = \left(\frac{n_{p,\text{fast}} v_{\text{SW,fast}}^2}{n_{p,\text{slow}} v_{\text{SW,slow}}^2}\right)^{\frac{1}{5.7}} = 0.98$$
(3)

for $v_{\text{SW,slow}} = 450 \text{ km s}^{-1}$ and $v_{\text{SW,fast}} = 600 \text{ km s}^{-1}$, and $n_{p,\text{slow}}/n_{p,\text{fast}} = 2$. Note that flaring parameters are altered in the same way as they are for the Voyager 2 data samples.

2.2. Neutral Particles in the System

Both exospheric and moon-sourced neutrals are considered in this study. There are no direct measurements of moon-sourced neutrals at Uranus, but modeling has been performed by Cheng (1987), henceforth C87, who estimated neutral source rates based on Voyager 2 plasma measurements, and Eviatar and Richardson (1986), henceforth ER86, who assumed the Uranian moons were Saturn-like and gave pre-Voyager estimates of minimal and maximal densities. C87 provides the radial extent and half thickness of the tori, as well as the lowest estimates of density while ER86 provides higher estimates. The three different values are considered to reflect the limited in situ knowledge of the Uranian system and its temporal variability. Seasonal configurations of the system are also incorporated into the model, with the half thickness acting in different planes for equinox and solstice, shown in Figure 2. At equinox, the equator is aligned with the Uranus-Sun line, meaning the tori are seen edge-on in the *y-z*

NAYLOR ET AL. 4 of 17



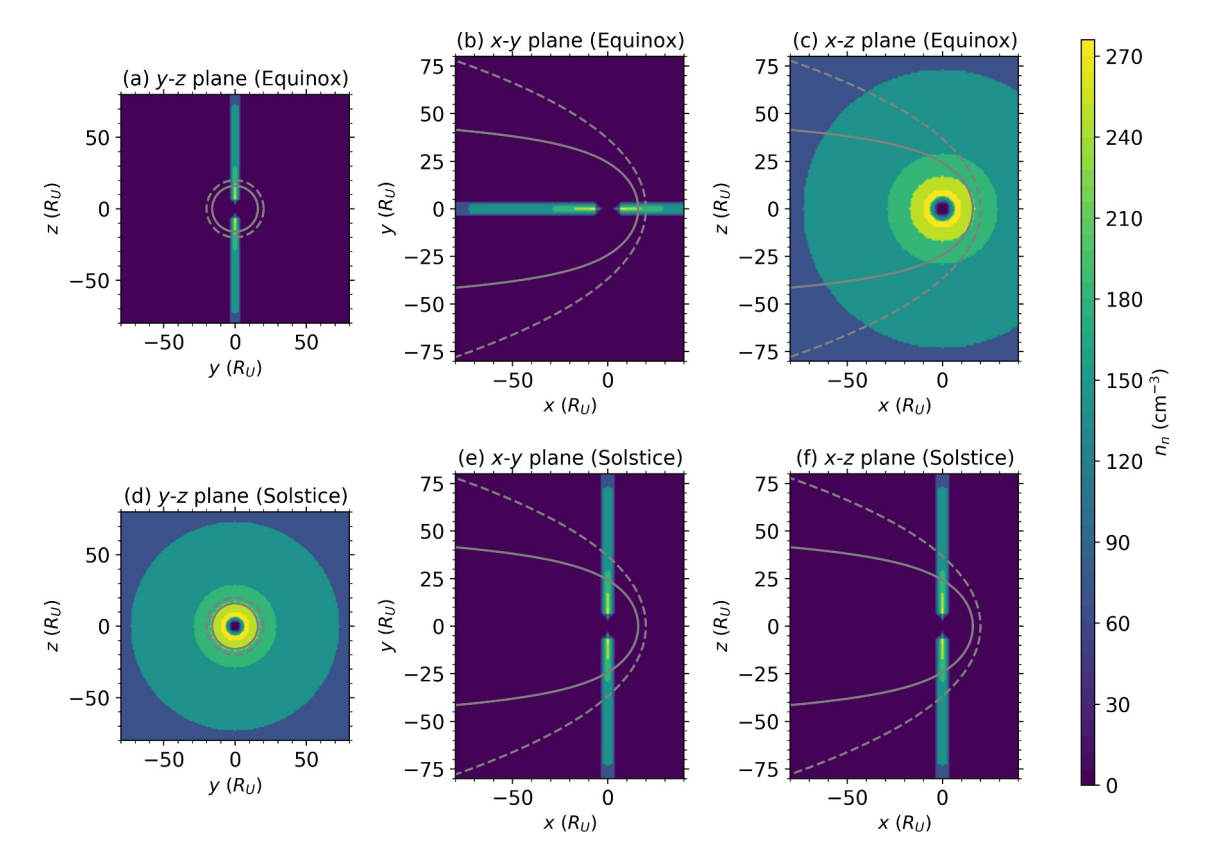


Figure 2. Moon-sourced neutral tori in the Uranian system at equinox and solstice. In this case, densities are taken from $n_{ER,max}$. At solstice, the tori are seen disk-on from the Sun and at equinox, they are seen edge-on. The magnetopause and bow shock surfaces are imposed in gray (bow shock dotted) to show the distribution of the neutrals within the magnetosheath.

plane, with the half thickness acting in the *y*-direction. At solstice, Uranus's rotation axis faces the Sun, meaning the disks of the tori are visible in the *y*-*z* plane, with the half thickness in the *x*-direction. Torus densities are held constant, in effect creating a "washer-like" structure for each moon. The half thickness is simplified, acting as the distance at which the torus cuts off, that is it acts as a jump condition where the density drops to zero. Figure 2 highlights that the tori extend past the edge of the magnetosheath during the default conditions, so even with significant expansion of the magnetosphere, X-ray emission will still be possible. Table 1 provides values for the size and density of each torus.

Table 1
Predicted Moon-Sourced Neutral Particle Densities in the Uranian Magnetosphere

Moon	$d(R_U)$	r (R_U)	r_+ (R_U)	$\Delta Z (R_U)$	$n_{\rm C87}~({\rm cm}^{-3})$	$n_{\rm ER,min}~({\rm cm}^{-3})$	$n_{\rm ER,max}~({\rm cm}^{-3})$
Miranda	5.1	2.9	9.9	0.38	0.06	1.16	30.68
Ariel	7.5	3.8	17	0.68	0.11	8.34	67.14
Umbriel	10.4	4.7	29	1.1	0.12	8.17	40.17
Titania	17.0	6.1	73	2.3	0.02	36.3	72.5
Oberon	22.8	6.9	150	3.6	0.002	50.5	69.8

Note. d, r_- and r_+ are the moon's radial distance from Uranus and inner and outer torus radii, respectively, in units of Uranian radii. ΔZ is the half thickness of the torus, n_{C87} is the neutral density as reported by Cheng (1987), and n_{ERmin} and n_{ERmin} are minimal and maximal neutral densities as reported by Eviatar and Richardson (1986). It is important to note that density values are predicted and have not been measured.

NAYLOR ET AL. 5 of 17

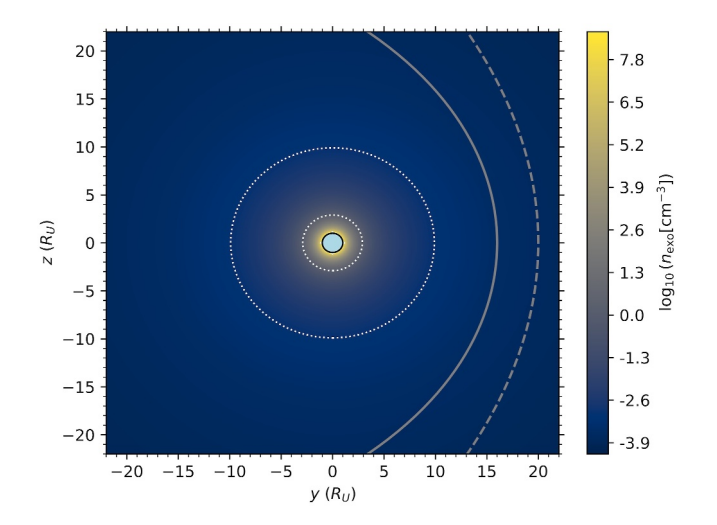


Figure 3. Exosphere of Herbert et al. (1987) shown in the *y-z* plane, with the inner and outer bounds of the torus of Miranda (the innermost moon) shown with the white dotted lines, and the magnetopause and bow shock surfaces in gray. Uranus is at the center and exospheric density quickly drops off. In the magnetosheath, exospheric density is negligibly low.

Uranus's exosphere is implemented using the work of Herbert et al. (1987) who gave exospheric density as

$$n_{\rm exo} = c_1 \exp\left(\frac{c_2}{r}\right) \tag{4}$$

where $c_1 = 4 \times 10^{-5} \text{ cm}^{-3}$, $c_2 = 31 R_U$ and r is the radial distance from Uranus in R_U .

Exospheric density is shown in Figure 3, along with the magnetopause and bow shock surfaces and the inner and outer boundary of the innermost moon torus, that of Miranda. While exospheric density is considerable at 2.9 R_U , r_- for the Miranda torus, by the outer edge of the torus, and even more so the magnetosheath, it is negligibly low.

2.3. Volumetric Emission Rate

The volumetric emission rate of soft X-rays from the magnetosheath is given as

$$P = \sum_{n} n_n n_q v_{\text{rel}} \sigma_{sqn} b_{sqj} \tag{5}$$

where n_n is the neutral density (with \sum_n reflecting the summation over the different neutral species present), n_q is the solar wind O^{7+} density (since only $O^{7+} \rightarrow O^{6+*}$ is considered in this model), v_{rel} is the relative velocity between the ions and neutrals, σ_{sqn} is the relevant charge exchange cross section and b_{sqj} is the branching ratio, that is the probability of a transition of interest occurring after charge exchange. Volumetric emission is given in photon cm⁻³ s⁻¹ (see e.g. Sibeck et al., 2018; Whittaker et al., 2016).

Relative velocity, v_{rel} is given by

$$v_{\rm rel} \sim \left(v_{\rm bulk}^2 + v_{\rm therm}^2\right)^{1/2} \tag{6}$$

where v_{bulk} is the bulk velocity of the ions, approximated as the solar wind velocity, and where v_{therm} is the thermal velocity of the ions, given by

$$v_{\text{therm}} = \sqrt{\frac{3k_BT}{m_p}} \tag{7}$$

where k_B is the Boltzmann constant, T is the solar wind ion temperature and m_p is the proton mass. The bulk and thermal velocities of the neutrals are negligible compared to ions. We approximate the magnetosheath velocity and temperature to be the same as the solar wind values. On the large scale, effective velocity within the magnetosheath is approximately equal to the solar wind velocity (Sibeck et al., 2018; Spreiter et al., 1966). Therefore, using the unshocked solar wind velocity throughout the magnetosheath is a reasonable approximation for this analysis, but it should be noted that changes in emission due to magnetosheath velocity variations will not be captured.

To calculate charge exchange rates, the abundance of O^{7+} relative to hydrogen in the solar wind is required. Whittaker and Sembay (2016) used 13 years of Advanced Composition Explorer (ACE) data to calculate oxygen ion abundances in the solar wind. They give slow and fast solar wind ion abundances, separated at $v_{SW} = 500 \, \text{km}$ s⁻¹. The most common abundances for O^{7+}/O and O/H give a relative abundance of O^{7+}/H of 1.48×10^{-5} and 6.99×10^{-6} for slow and fast wind, respectively.

Cross sections are taken from the work of Bodewits et al. (2007) and Schwadron and Cravens (2000), who provide hydrogen-like and oxygen-like cross sections, respectively. Bodewits et al. (2007) provides cross sections for

NAYLOR ET AL. 6 of 17



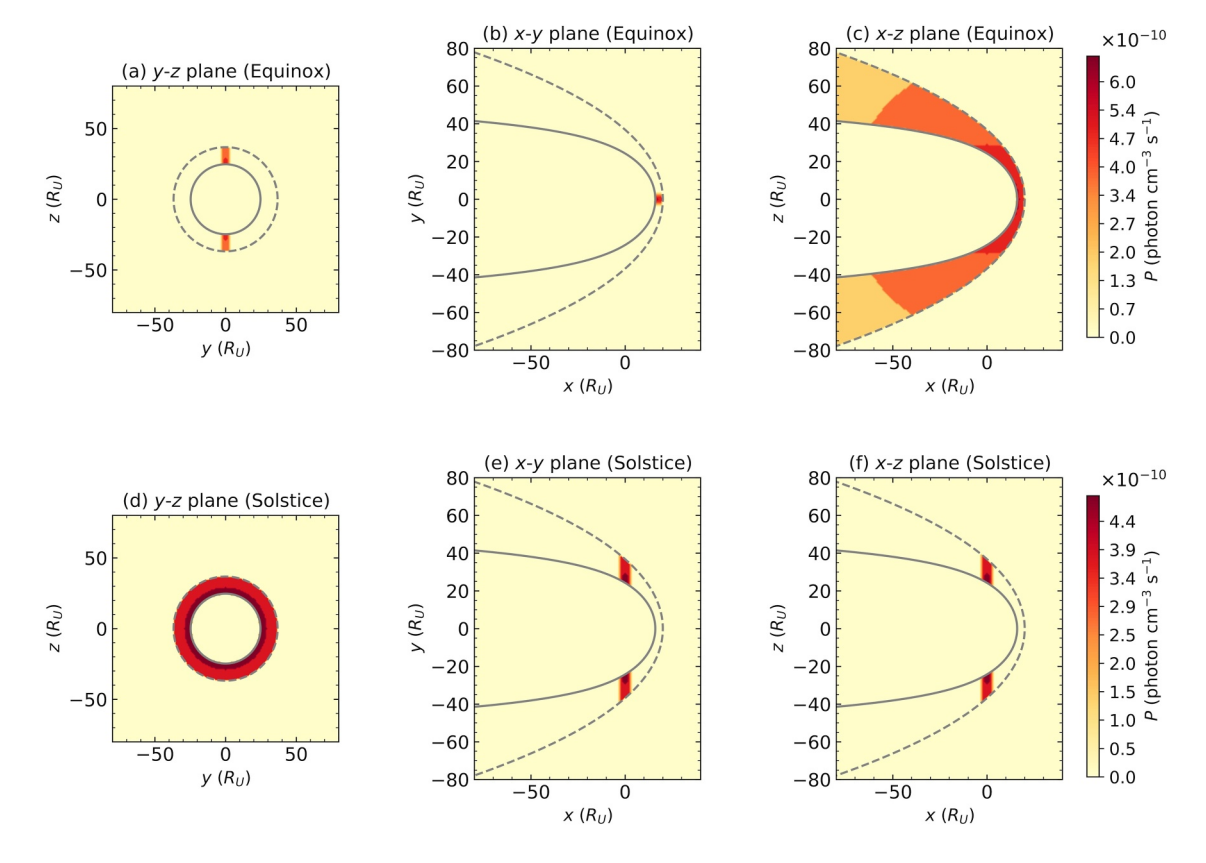


Figure 4. Slices of volumetric emission rate in the y-z, x-y and x-z planes (a, b, c, d, e, and f) in the case of $v_{SW} = 450 \text{ km s}^{-1}$ and for the Eviatar and Richardson (1986) model maximal neutrals, considered at both equinox (top) and solstice (bottom). Magnetopause and bow shock surfaces for default solar wind conditions are shown in gray, with the bow shock dotted. Emission is generated where there is intersection between the magnetosheath and the neutral tori.

interactions between O^{7+} and hydrogen-like neutrals, given as 5.85×10^{-15} cm⁻² for slow wind and 5.6×10^{-15} cm⁻² for fast wind. Schwadron and Cravens (2000) provide a constant cross section value for interactions between O^{7+} and oxygen-like ions by taking the cross section for H_2O interactions and assuming it is similar for oxygen. The value is stated as 12×10^{-15} cm⁻². As a simple estimation, at Uranus, 1/3 of the moon-sourced neutrals are hydrogen based and 2/3 are oxygen based (following ER86).

2.3.1. Baseline Results

Figure 4 shows the baseline volumetric emission rate results, that is emission rates at the default conditions using the maximal neutrals of ER86. Emission rates are calculated to be on the order of 10^{-10} photon cm⁻³ s⁻¹ at both equinox and solstice. The different planes show emission is generated where the neutrals are intersecting the magnetosheath. For example, at equinox, in the *y-z* plane (along the Uranus-Sun line), two bands of emission are seen where the neutral tori intersect with the sheath, but at solstice, where the tori are disk-on to the Sun, a corresponding disk of emission is seen. For $n_{\text{ER,max}}$, volumetric emission peaks at 6.64×10^{-10} photon cm⁻³ s⁻¹ and 4.85×10^{-10} photon cm⁻³ s⁻¹ for equinox and solstice, respectively.

2.4. Flux and Integration Times

The intensity of soft X-rays emitted from the magnetosheath along a line of sight is given by

$$I = \int P \frac{d\Omega}{4\pi} dl = \frac{1}{2} \int P dz \tag{8}$$

Which is approximated as the sum of the volumetric emission along the z-axis (meaning images are top down to the system, in the x-y plane), with dl = dz. The $d\Omega$ term integrates to 2π , meaning intensity overall has a 1/2 term

NAYLOR ET AL. 7 of 17



Table 2
Configurations of the SMILE (Sembay et al., 2024), LEXI (Walsh et al., 2024) and Future SXIs Used to Investigate Flux Detection and Minimum Integration Times Upon Approach to Uranus

			Imaging distance	
SXI	FOV	$A_{\rm effective}~({\rm cm}^2)$	R_U	au
SMILE	26.5° × 15.5°	9.6	212	0.630
LEXI	$9.1^{\circ} \times 9.1^{\circ}$	44.18	628	1.87
Future	$53^{\circ} \times 31^{\circ}$	100	100	0.297

Note. Imaging distance is the minimum radial distance from the system at which the SXI can image the whole magnetosheath within its field-of-view.

to reflect that only forward facing emission is being considered. Volumetric emission rate is scaled for distance to the SXI $(1/d^2)$ to give intensity at the SXI and multiplied by dxdy (where $dx = dy = 1R_U$) to give the flux, F, detected at the SXI from a grid cell. The SXI is placed sufficiently far from Uranus to image the whole model domain. The distance from Uranus to the SXI required to image the whole system is thus dictated by trigonometry:

$$d_{\text{SXI}} = \frac{50 R_U}{\tan(\text{FOV}_{\text{SXI}}/2)} \tag{9}$$

50 R_U reflects half of the x-domain, with a dayside standoff distance of $\sim 20 R_U$ and a nightside magnetotail of 80 R_U . The distance from each grid cell to the SXI is thus:

$$d_{\text{CelIToSXI}} = \sqrt{(d_{\text{SXI}} - z)^2 + x^2 + y^2}$$
 (10)

Count rate is given by

$$C = I \times a_{\text{eff}} \tag{11}$$

where $a_{\rm eff}$ is the effective area of the SXI. The integration time required to detect one photon is then

$$\tau_{\rm int} = \frac{1}{F} \tag{12}$$

We consider three imagers: SMILE-like, LEXI-like, and a "future" technology SXI, with double the FOV of SMILE and an effective area of $100 \, \mathrm{cm^2}$. This technology might exceed mass and space constraints on the Uranus orbiter mission, but it is useful to consider given the system sizes in the outer solar system. The specifications and distance required for SMILE (Sembay et al., 2024), LEXI (Walsh et al., 2024) and the future imager are shown in Table 2. It is important to note that detailed analysis of whether imaging is possible is not performed in this study. Rather we make simple estimates of integration times and comparing these times to system timescales to explore whether an SXI imager could provide physical insight into magnetospheric dynamics.

2.4.1. Viewing Geometry

The position at which the SXI observes the system affects flux detection and must be considered for mission viability. Figure 5 shows the modeled flux images from three viewing positions, comparable to the three volumetric emission slices shown in Figure 4: along the Uranus-Sun line, top-down and side-on. The equatorial (top-down) view is used for all flux and integration time estimates in this model. This is because for a front-on view, that is approaching down the planet-Sun line, reflected emission from the disk of the planet can be a significant background source. It is not known how much Uranus will contribute to the background, but a top-down or side-on view reduces it regardless. Additionally, given Uranus's axial tilt, a side-on approach corresponds to a polar orbit. These are more difficult to achieve and keep stable than an equatorial orbit (Wertz & Larson, 1999). While the spacecraft would approach the system side-on, an orbital mission would then likely assume a top-down view for the majority of the mission. Therefore, a top-down view is chosen and used throughout the study.

3. Parameter Investigation

3.1. Neutral Density Model

Table 3 reports volumetric emission rates (P) and integration times ($\tau_{\rm int}$) for the different models of moon-sourced neutral density, at equinox and solstice. It also presents the number of photons that could be detected within a quarter of a planetary rotation ($N_{1/4}$, 17.24 hr/4 = 4.31 hr). This is because observing one photon would not be sufficient for imaging the system. While detailed analysis of imaging possibilities is not considered in this model, integration times are compared to the planetary rotation period through $N_{1/4}$ in order to make some

NAYLOR ET AL. 8 of 17



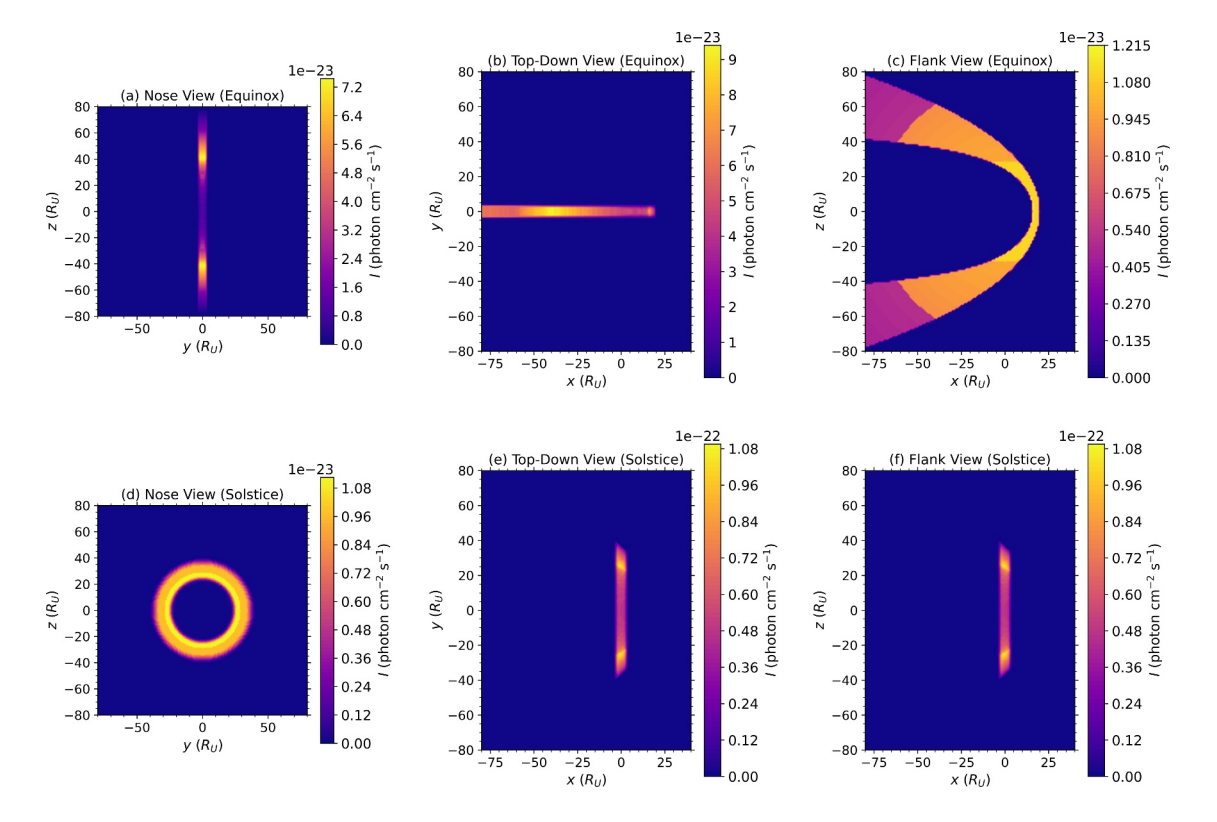


Figure 5. Intensity images for a SMILE-like SXI from different viewing geometries at (top row) equinox and (bottom row) solstice: (a/d) front-on, (b/e) top-down and (c/f) side-on. A top-down view is used throughout this study to avoid reflected emission from the disk of the planet and due to equatorial orbits being easier to achieve and stabilize than polar orbits (Wertz & Larson, 1999). The different panels show that the amount of flux detected is dependent on viewing position.

inferences on the capability of the SXI in illuminating dynamic system behavior. For all cases, volumetric emission is higher at equinox than at solstice because the tori intersect the nose of the magnetopause at small distances, leading to a higher density of neutrals within the magnetosheath.

Neutrals at Uranus are not well understood, so it is important to consider the ranges of emission rates obtained when using the different neutral density models. The baseline results, using $n_{\rm ER,max}$, discussed in Section 2.3.1, obtain emission on the order of 10^{-10} photon cm⁻³ s⁻¹. This corresponds to detected flux and integration times of 6.00×10^{-4} photon cm⁻² s⁻¹ and 0.0482 hr at equinox, and 6.95×10^{-4} photon cm⁻² s⁻¹ and 0.0416 hr for solstice. It is noteworthy that even though emission is higher at equinox than solstice, flux detection is higher at solstice in this case. This is because of the equatorial position of the SXI - the line-of-sight integration is higher when the neutral tori are in the solstice configuration. Using the C87 neutrals, maximum emission rate is on the order of 10^{-13} photon cm⁻³ s⁻¹, leading to high integration times on the order of tens of hours. This is far greater

Table 3Table Presenting Mean and Maximum Volumetric Emission (P, in Photon cm⁻³ s⁻¹), As Well As Minimum Integration Time $(\tau_{int}, in Hours)$ and the Number of Photons Imaged Within a Quarter of a Planetary Rotation $(N_{1/4}, 4.31 \text{ hr})$ at Equinox and Solstice for the Different Moon-Sourced Neutral Particle Models in the Uranian System

	Equinox			Solstice		
Neutral model	P (photon cm ⁻³ s ⁻¹)	$ au_{ ext{int}}$ (h)	$N_{1/4}$	P (photon cm ⁻³ s ⁻¹)	τ_{int} (h)	$N_{1/4}$
Cheng	6.71×10^{-13}	68.5	0	3.78×10^{-13}	75.7	0
ER Min	2.76×10^{-10}	0.0785	54	2.54×10^{-10}	0.0740	58
ER Max	6.64×10^{-10}	0.0482	89	4.85×10^{-10}	0.0416	103

Note. First used is n_{Cheng} , then the $n_{\text{ER,min}}$ and $n_{\text{ER,max}}$ values at 5 eV from Eviatar and Richardson (1986). In all three cases, the exosphere of Herbert et al. (1987) is also included but has a negligible effect on emission. Flux is obtained from imaging the system top-down.

NAYLOR ET AL. 9 of 17



than the rotation rate of Uranus and the timescales over which the solar wind varies in density, temperature and speed. If the neutral densities at Uranus are on the order of n_{Cheng} , then soft X-ray imaging would likely not be a useful method to explore magnetospheric dynamics. However, we note that the work of Jasinski et al. (2024) suggests that Uranus was most likely in a plasma-depleted state during the Voyager 2 flyby; n_{Cheng} was based on Voyager 2 plasma measurements, so it is possible that more common states of Uranus's magnetosphere contain more neutrals than what was extrapolated by Cheng (1987). The ER86 model also estimated minimal neutral densities, which also produce volumetric emission rates on the order of 10^{-10} photon cm⁻³ s⁻¹ and give integration times of less than 0.1 hr (when the solar wind conditions of Tóth et al. (2004) are imposed). These values allow multiple photons (~100 at equinox) to be imaged within a quarter of a planetary rotation, providing a useful diagnostic for system behavior. The most important point that these results present is that while neutral densities at Uranus are poorly understood (with no Voyager 2 measurements), there is a considerable range in the possible values that can lead to significant emission rates over a planetary rotation. So even if, for example, there is only a fraction of $n_{\text{ER,max}}$ commonly found at Uranus, it may still be sufficient for soft X-ray imaging to be useful. Without the moon-sourced neutrals, however, the case for soft X-ray imaging at Uranus is much weaker.

For this model, even though exospheric density is included in emission calculations, it does not have any considerable contribution to driving emission (due to being negligibly low in the magnetosheath). Hence, the moon sourced neutrals are the most important contribution to the system, especially those of Ariel, Umbriel and Titania, whose tori are located such that they intersect with the magnetosheath.

In order to be useful for imaging, soft X-rays emitted from magnetosheath must be detected at a higher intensity than emission from other sources. Other sources of soft X-ray emission include the Sun (see review by Sibeck et al., 2018), as well as interstellar neutrals crossing the heliopause exchanging charge with the solar wind (Cravens, 2000). Many planetary environments also have soft X-ray emissions, caused by various processes. For example, charge exchange between magnetospheric ions and exospheric neutrals produces soft X-ray aurora at Jupiter (Cravens et al., 1995, 2003; Metzger et al., 1983). There are also sources beyond the solar system including galaxies (e.g., Snowden et al., 1990; Kuntz & Snowden, 2000) as well as emissions from point sources including stars, active galactic nuclei and pulsars. The cosmic diffuse soft X-ray background (Giacconi et al., 1962) has been well mapped (Snowden et al., 1997) and is temporally fairly constant, meaning it can be removed from results to obtain a calibrated observation of the magnetosheath. Point sources can be more difficult to remove but are generally much dimmer. Sibeck et al. (2018) showed that the terrestrial magnetosheath is still visible in soft X-rays when background sources are considered. This study does not consider the background sources so further work must be undertaken to better understand imaging viability when background sources are included. The modeled intensity images presented in this study can be considered to be similar to what the calibrated images may look like. Previous attempts to observe Uranus in X-rays by Chandra were not able to confirm unambiguous detections, but the Uranus-region was significantly brighter than the background (Dunn et al., 2021). While further investigation will be needed to ensure the soft X-ray emission from the magnetosheath is distinguishable from the background, Kuntz and Snowden (2000) discuss that the soft X-ray background is mostly in the 1/4 keV band, while O⁷⁺ solar wind charge exchange-induced soft X-ray emission has spectral lines around 0.56 keV (Koutroumpa et al., 2006). Therefore, for this study (that focusses only on O⁷⁺), the soft X-ray background is unlikely to be an important factor.

3.2. Solar Wind Driving

Solar wind conditions are varied in three different scenarios to test how emission rates change, with results presented in Table 4. All subsequent results use the maximal neutral densities of Eviatar and Richardson (1986), as neutral densities at Uranus are under-constrained. Volumetric emission rates and fluxes will be lower for the minimal neutrals of Eviatar and Richardson (1986) or Cheng (1987), the degree to which indicated in Table 3. First tested is a case of fast solar wind, where speed is increased to 600 km s^{-1} and proton density is halved. This affects the magnetopause and bow shock shapes through variations in the standoff distances and flaring parameters. Ion temperature is kept fixed to the Tóth et al. (2004) value in this case. Emission rate is lower than the slow wind case, maximizing at 1.99×10^{-10} photon cm⁻³ s⁻¹ and 1.45×10^{-10} photon cm⁻³ s⁻¹ for equinox and solstice respectively. Integration times are noticeably higher, at 0.160 and 0.139 hr for equinox and solstice respectively.

An increase in emission for fast solar wind could be expected due to the increased bulk flow speeds of solar wind ions and compression of the magnetosphere leading to higher neutral densities coincident with the magnetosheath

NAYLOR ET AL. 10 of 17



Table 4Table of Volumetric Emission Rate, P (Photon cm^{-3} s^{-1} , Integration Times, τ_{int} (h) and Number of Photons Imaged in a Quarter of a Planetary Rotation (4.31 hr), $N_{1/4}$, for Variations of the Solar Wind Conditions That Were Tested in Section 3.1

	Equinox			Solstice		
SW state	P (photon cm ⁻³ s ⁻¹)	τ_{int} (h)	$N_{1/4}$	P (photon cm ⁻³ s ⁻¹)	τ_{int} (h)	$N_{1/4}$
Fast wind	1.99×10^{-10}	0.160	26	1.45×10^{-10}	0.139	31
V2 _{inbound}	1.00×10^{-10}	0.222	19	7.83×10^{-11}	0.174	24
V2 _{outbound}	5.64×10^{-10}	0.0569	75	4.12×10^{-10}	0.0506	85

Note. "Fast wind" represents testing solar wind where $v_{\rm SW} = 600~{\rm km~s^{-1}}$ and $n_p = 0.05~{\rm cm^{-3}}$ (and other parameters are the same as previously, from Tóth et al. (2004)). V2_{inbound} represents a sample of Voyager 2 data taken from Jasinski et al. (2024), where $v_{\rm SW} = 435~{\rm km~s^{-1}}$, $n_{\rm SW} = 0.0214~{\rm cm^{-3}}$ and $r_{\rm MP} = 20.3~R_U$, taken before Voyager 2 crossed the Uranian bow shock. V2_{outbound} represents another sample of Voyager 2 data, taken after the spacecraft had crossed back over the bow shock. In this case, $v_{\rm SW} = 428~{\rm km~s^{-1}}$, $n_{\rm SW} = 0.0892~{\rm cm^{-3}}$ and $r_{\rm MP} = 15.9~R_U$.

location. However, there is an offset to consider as the abundance of O^{7+} in the solar wind is approximately an order of magnitude lower in the fast regime than the slow, and proton density decreases too. The discrete modeling of the neutral tori mean that compression of the magnetosphere does not change the density in the magnetosheath, so only the increase in relative velocity between the ions and neutrals acts against the decrease in proton density and heavy ion abundance. Hence, for the simple "slow-fast" comparison, there is decrease in emission in the fast wind case when compared to the slow wind. However, it is important to note this simply examines the change in emission due to the change of speed and composition of the solar wind. Realistically, there are further differences between the two regimes that must be accounted for to give the full picture of emission changes. It is clear that further development of the neutral densities is crucial, as it is unlikely to be constant across each torus, especially the large tori of Titania and Oberon. This would allow a more thorough investigation into how changes in solar wind conditions affect emission.

Next tested is a sample of Voyager 2 data taken from Jasinski et al. (2024), where $v_{\rm SW}=435~{\rm km~s^{-1}},$ $n_p=2.14\times10^{-2}~{\rm cm^{-3}}$ and $r_{0,\rm MP}=20.3~R_U$, and solar wind temperature remains at $5.45\times10^3~{\rm K}$. This measurement was taken in the weeks leading up to Voyager 2's crossing of the Uranian bow shock. Emission rates in this case maximize at 1.00×10^{-10} photon cm⁻³ s⁻¹ for equinox and 7.92×10^{-11} photon cm⁻³ s⁻¹ for solstice. This gives minimum integration times of 0.222 and 0.174 hr for equinox and solstice respectively, which is significantly higher than both the slow and fast wind cases. Here, the proton density is considerably lower than the default value ($\sim0.02~{\rm cm^{-3}}$ compared to $0.1~{\rm cm^{-3}}$) which causes a significant decrease in emission. Realistically, the solar wind conditions are very changeable at any point in the heliosphere, so their effects on emission will need to be further investigated. At equinox, only two photons are predicted to be imaged within a quarter of a planetary rotation, reducing the viability of the SXI as a useful tool for investigating system dynamics.

Another sample of Voyager 2 data is considered, from after the outward crossing of the bow shock. In this case, $v_{\rm SW}=428\,{\rm km\,s^{-1}}$, $n_{\rm SW}=0.0892\,{\rm cm^{-3}}$ and $r_{\rm MP}=15.9\,R_U$. These solar wind conditions are closer to the default ones, meaning emission rates and integration times return to the higher values not seen in the first Voyager 2 sample. This presents the case that solar wind ion density is an important driver of emission along with neutral density. The significant expansion of the magnetosphere due to the reduced dynamic pressure of the solar wind (moving the magnetopause standoff distance $\sim 4\,R_U$ forward) means that the torus of Ariel is no longer within the magnetosheath. Solar wind speed is in the slow regime for both samples and the difference is too small to drive any significant emission changes (7 km s⁻¹), it therefore is the combination of the decrease in neutral density and ion density that lead to a significant reduction in emission rate.

Investigations into how other solar wind properties, such as temperature variations, affect emission are useful, especially when considering that by the time the solar wind reaches Uranus, it is more often in the slow regime than fast (e.g., Belcher et al., 1993), so comparisons between slow and fast wind may not be supported by regular observations. The samples of Voyager 2 data do not include solar wind temperature so it has been kept fixed at the value used in the Tóth et al. (2004) model, 4.7 eV. However, this is not necessarily a problem, as temperature is only incorporated into this model through the relative velocity calculation which includes a thermal velocity term. At a magnetosheath solar wind temperature $T_{\rm SW}=4.7$ eV, thermal velocity is

NAYLOR ET AL. 11 of 17



Table 5Integration Times (τ_{int}) (h) and Number of Photons Imaged in a Quarter of a Planetary Rotation (4.31 hr, $N_{I/4}$) at Equinox and Solstice for the SMILE and LEXI (Walsh et al., 2024) SXIs and a Hypothetical Future SXI With Double the FOV of SMILE and an Effective Area of 100 cm²

	Equino	K	Solstice	;
SXI Configuration	$ au_{ m int}$ (h)	$N_{1/4}$	$ au_{ m int}$ (h)	$N_{1/4}$
SMILE	0.0482	89	0.0416	103
LEXI	0.102	42	0.0793	54
Future SXI	7.94×10^{-4}	5,428	8.89×10^{-4}	4,848

Note. SMILE's Integration times are included for completeness but they are no different from those reported in Table 1 under "ER Max."

$$v_{\text{therm}} = \sqrt{\frac{3k_BT}{m_p}} \sim 36.7 \text{ km s}^{-1} < v_{\text{bulk}} = 450 \text{ km s}^{-1}$$
 (13)

so the bulk velocity dominates the equation and temperature variations will only have small effects on emission rate. Therefore, solar wind density is a stronger driver of emission than temperature. This, while true in this model, does not take into account the full physics of the solar wind. For example, higher temperatures may lead to higher charge state distributions and enhanced charge exchange cross sections, leading to double capture etc. Clearly, a more thorough physical treatment of the solar wind at different temperatures would be required for a full investigation into its driving of emission.

3.3. SXI Configurations

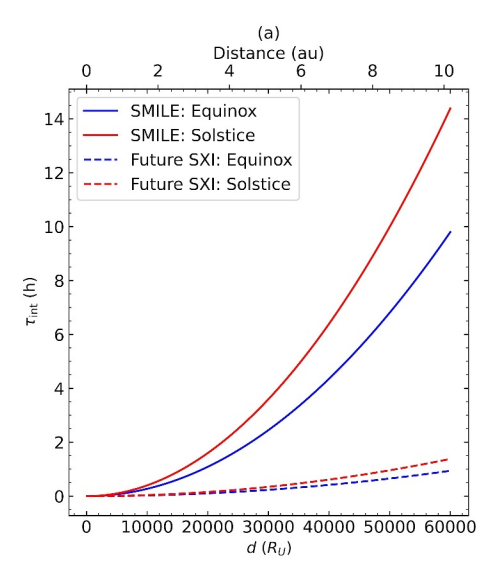
Finally, modifications to the SXI's imaging capabilities are considered. Until now, the SXI has been considered to be SMILE-like, with the FOV and effective area described in Section 2.4 in Table 2. Table 5 presents the integration times and photons detected during a quarter of a planetary rotation for LEXI-like and future SXI. It shows that when using a LEXI-like SXI, the minimum integration time increases in both the equinox and solstice cases, but the future SXI leads to a decrease of 2 orders of magnitude. For the future SXI, the integration time at both equinox and solstice is approximately 3 s - this allows for the imaging of many photons (on the order of 10^4) to be imaged within a planetary rotation, unlocking the possibility of continuous imaging of the magnetosheath within timescales of, for example, rapid solar wind dynamic pressure variations.

Integration timescales are lowest for the future SXI, then SMILE, and highest for LEXI. This is expected as even though LEXI has a higher effective area than SMILE (Walsh et al., 2024; Sembay et al., 2024), the lower FOV dominates and means it must be at a larger minimum approach distance to image the whole system, using the simple trigonometric approximation for imaging. SMILE and LEXI are the most up-to-date SXI technology available, but are suited for use at Earth, not the much bigger systems of the outer planets. Therefore the future SXI, while perhaps ambitious with its configurations, is good to consider as an instrument onboard an outer planetary mission as it is modified to observe larger magnetospheres. The 100 cm² effective area is not out of the realm of possibility for future imagers, and several X-ray instruments already have areas around 50 cm², including LEXI (Walsh et al., 2024) and MIXS, the Mercury Imaging X-ray Spectrometer, onboard the BepiColombo mission to Mercury (Fraser et al., 2010). That said, it is important to consider that there is a trade-off between effective area and FOV - but the results obtained here are high enough to allow for reduction in FOV or $A_{\rm eff}$ while maintaining reasonable integration times. The integration times of a LEXI-like SXI could be improved by allowing a closer approach distance and focusing the imaging on a smaller part of the system. This may be useful at or close to equinox, where the flux is only detected in a narrow band due to the edge-on nature of the tori. Closer imaging may allow for better investigation of this area rather than having an image of largely zero flux detection. That said, all of the SXIs perform well, with the worst case scenario (LEXI at solstice) still imaging several photons within a planetary rotation. This demonstrates that current SXI technology is potentially able to image Xray emission at Uranus and fulfill the science objectives to understand solar wind coupling with the magnetosphere, although improvements in technology would provide more insight into rapidly occurring dynamics.

Figure 6 shows how minimum integration times change with SXI distance from the system, using a point source approximation. The SMILE and future SXIs are considered. LEXI is not because its minimum imaging distance is $\sim 900~R_U$. Figure 6a shows that by $60,000~R_U \sim 10$ au, integration times are still fairly low, remaining under the planetary rotation period for both SXIs, at both equinox and solstice. Figure 6b shows distance within $2000~R_U$ to consider the view approaching orbital insertion. Out to $2,000~R_U$, integration times for both SXIs remain under $\sim 10^{-2}$ h, on the order of seconds. This makes a good case for imaging possibilities by an orbiter, but it should be noted that these times are underestimates due to the use of the point source approximation close to the system.

When using the point source approximation, integration times remain fairly low even at very high approach distances such as $60,000 R_U \sim 10$ au. If the spacecraft is traveling at an average speed of 20 km s^{-1} , it would take ~ 868 days to cover this distance. In this time, the SXI could be turned on and preliminary imaging could be

NAYLOR ET AL. 12 of 17



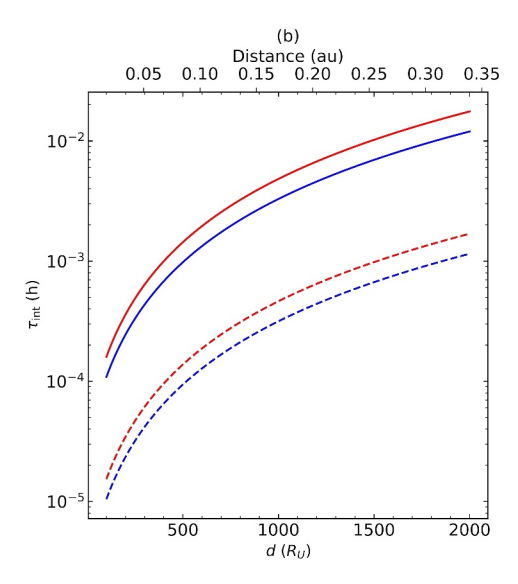


Figure 6. (a) Integration time in seconds as a function of SXI distance (in units of R_U and au), using the SMILE and future SXI configurations. This uses a point source approximation and shows that even at very high distances, up to $10,000~R_U\sim 1.7$ au, integration times remain within system timescales. It suggests that the SXI could be turned on during its approach to Uranus, long before it gets close to the system, in order to make preliminary imaging efforts. (b) The first $2000~R_U$ of (a), with a \log_{10} scale used for integration time to show what happens for a spacecraft in orbit (thought it must be noted that the point source approximation becomes less valid at closer distances to Uranus).

performed - while there would not be any spatially distributed images taken, changes in the flux arriving at the SXI could potentially give some early indications of the drivers of soft X-ray emission. At such far distances, the point source approximation is valid to use, but it is important to consider that at 10 au, the spacecraft could be closer to Saturn than Uranus, which could lead to contamination, depending on solar system configuration.

Figure 6a shows that at distances up to 10 au, the future SXI's integration times remain around 1 hr/photon. This is too high for imaging to be viable, but an instrument with a higher effective area such as the Earth-orbiting XMM-Newton telescope or Chandra X-Ray Observatory may be able to detect photons from the magnetosheath, at a distance of ~18 au from Uranus. However, due to the changing configuration of the Uranian magnetosphere over diurnal timescales (for example, Cao and Paty (2017), the magnetosheath is unlikely to be fixed in one position long enough for sufficient photon detection above background levels, and may not be distinguishable from the X-ray background when observed from Earth. Estimating the flux from Earth-based observations using a full dynamical model that includes cusps is left for a future study.

3.4. Sources of Underestimation

While the results point to there being a significant amount of emission from the magnetosheath, it is important to consider that there are many unknowns and this is a simplified description of the magnetosphere. Specifically, cusps may play a large role in X-ray emission as they allow deep penetration of solar wind into the magnetosphere where neutral densities are high - even the exospheric density may play an important role here. Large exospheric densities close to Uranus combined with increasing ion densities as solar wind is funneled into the cusps suggest that emission could be higher than predicted in this analysis. Due to the large tilt of the magnetic axis from Uranus's spin axis (\sim 60°), the cusps are often in unusual configurations when compared to a terrestrial-like magnetosphere (e.g., Cao & Paty, 2021). Furthermore, the extreme tilt and magnetic field induce large variations in clock angle, even under steady solar wind conditions, which affect reconnection rates. An important consideration which we have not explored here is the phase during Uranus's rotation when its magnetic pole faces into the solar wind. This results in the cusp facing into the solar wind (Jasinski et al., 2022) which may lead to very high emission rates. At equinox, the neutral tori may also intersect with the cusps edge-on, driving emission higher similarly to how it does for the sheath, seen in this study. Furthermore, a realistic description of the magnetopause must incorporate several factors, including the axial tilt of Uranus and the tilt of the magnetic axis from the rotation axis. These will lead to an asymmetrical magnetopause that can not be described by the bullet

NAYLOR ET AL. 13 of 17



shape of the Shue et al. (1997) model. Furthermore, seasonal changes affect only the neutral tori under the simplifications of this model. But in reality, the magnetopause is likely to be altered by these changes. The Voyager 2 flyby occurred when Uranus was very close to solstice, and the differences between the seasons will not be completely understood until another spacecraft investigates Uranus, although modeling suggests that magnetospheric variations are dependent on season (Cao & Paty, 2017).

Furthermore, cascades of emission and charge exchange between non- O^{7+} ions that have not been considered here will lead to further emissions. For instance, while O^{7+} charge exchange to O^{6+*} has been considered in this model, O^{8+} to O^{7+*} has not been considered (although it is important to note that the abundance of O^{8+} in the solar wind is considerably lower than that of O^{7+} , being approximately an order of magnitude lower in the slow solar wind (Whittaker & Sembay, 2016)). While it is not known the exact effect that including O^{8+} charge exchange will have on the calculated emission rates, the work of Xu et al. (2024) shows that at the terrestrial dayside magnetopause, the modeled ratio of integrated X-ray intensity of O^{7+}/O^{8+} ranges between 1 and 1.2—thus including O^{8+} has the potential to double the integrated X-ray flux.

Additionally, there are other species of ions in the solar wind that charge exchange with neutrals including highly charged carbon and nitrogen, and more (e.g., Liang et al., 2021). The AtomDB atomic charge exchange (ACX) model (http://www.atomdb.org/CX) (Smith et al., 2012, 2014) was used to make a simple charge exchange spectrum and count rate estimation considering oxygen only, which was then compared with estimates considering the full solar wind spectrum, considering ionic abundances from Wibisono et al. (2020); von Steiger et al. (2000). For a given ionic abundance, ACX determines charge state distributions from thermal energy, and calculates a best fit line spectrum (Dunn et al., 2020). The model predicts a factor of ~ 3.5 difference between the full and oxygen-only spectra (for further details, see Supporting Information S1). Therefore, full consideration of solar wind charge exchange may increase count rates significantly, potentially affecting imaging feasibility. Overall, we anticipate that for each neutral model considered, the emission rates estimated are a lower limit to what is generated within the Uranian magnetosheath.

4. Conclusions

This study presents the first model of soft X-ray emission from Uranus's magnetosheath. Simple bullet-shaped magnetopause and bow shock surfaces are imposed, estimated from Voyager 2 crossing data and from the model of Shue et al. (1997). Neutral tori are generated based on the predictions of Eviatar and Richardson (1986) and modeling of Cheng (1987). Soft X-ray volumetric emission rates are tested under the different neutral density values, at equinox and solstice. Solar wind conditions are then varied with the neutral density fixed at the most favorable value. Finally, different soft X-ray imagers (SXIs) are tested in order to understand which may be best suited for outer planetary missions. SXIs similar to those to be used on the SMILE (Sembay et al., 2024) and LEXI (Walsh et al., 2024) missions are tested as well as a future SXI with double the FOV and effective area of that of SMILE. We find:

- 1. Neutral density is the largest driver of emission but also the biggest unknown in the system. Using the model of Cheng (1987) emission is on the order of 10⁻¹³ photon cm⁻³ s⁻¹ (with Voyager 2-like solar wind conditions (Tóth et al., 2004)). Under both the minimal and maximal values given by Eviatar and Richardson (1986), emission is on the order of 10⁻¹⁰ photon cm⁻³ s⁻¹. Here, integration timescales are much less than a planetary rotation under both equinox and solstice configurations. Therefore, while the neutrals at Uranus are not well understood, there is a range of possible values that may lead to significant emission rates.
- Volumetric emission rates are higher at equinox than solstice due to the configuration of the neutral tori at the two points, but due to the top down approach of the instrument, flux detection at solstice is higher than at equinox.
- 3. Volumetric emission rates remain on the order of 10^{-10} photon cm⁻³ s⁻¹ for the fast wind ($v_{\rm SW}=600~{\rm km~s^{-1}}$) and a Voyager 2 data sample (taken after the Uranus flyby) but drop to 10^{-11} photon cm⁻³ s⁻¹ at solstice for another Voyager 2 sample (Jasinski et al., 2024), taken from 2 weeks before the Voyager 2 flyby when solar wind proton density was $\sim 20 \times$ lower than during the flyby itself. Correspondingly, integration times are higher in the low density case.
- 4. SMILE performs better than LEXI due to the higher FOV of SMILE which is advantageous for imaging the whole system at a closer distance.

NAYLOR ET AL. 14 of 17



- 5. All SXIs perform well under a point source approximation, with integration times remaining under 17 hr at $60,000 R_U \sim 10$ au.
- 6. Presented emission rates are likely underestimates due to several factors not having been considered, including the magnetospheric cusps and emission due to ions other than O⁷⁺

Overall, this work demonstrates that further development of the model is warranted and may lead to a better understanding of Uranus's magnetosheath and the role of X-ray emissions in the solar system. It indicates that soft X-ray imaging could be a potentially valuable tool on the Uranus orbiter mission, to allow remote, global and dynamic sensing of the magnetosheath and dayside cusp region. The next major stage of development will include moving from a simple, bullet-shaped magnetopause to a more realistic, asymmetrical magnetopause with the inclusion of cusp regions. Other developments will include development of the neutral tori from the washer-like state they are currently in, improvements to the magnetosheath conditions which are currently highly simplified, and looking at solar wind variations over more continuous timescales rather than looking at discrete data samples. Furthermore, charge exchange will be extended to consider non-O⁷⁺ ions and cascades of emission will be included in the model, increasing volumetric emission rates.

Acronyms

ACX	Atomic charge exchange
C87	Moon-sourced neutral density model of Cheng (1987)
ER86	Moon-sourced neutral density model of Eviatar and Richardson (1986)
FOV	Field-of-view
LEXI	Lunar environment heliophysics X-ray imager
MIXS	Mercury imaging X-ray spectrometer
SMILE	Solar wind-magnetosphere-ionosphere link explorer
SXI	Soft X-ray imager

Conflict of Interest

The authors declare no conflicts of interest relevant to this study.

Letters, 48(4), e2020GL091273. https://doi.org/10.1029/2020GL091273

Data Availability Statement

Model output files are available at Naylor et al. (2025). Files show the value of parameters at each point in the model grid.

Acknowledgments References

D.N. was supported by an STFC Studentship to Lancaster University. L.C. R. was supported by STFC Grant ST/Y002148/1 to Lancaster University. W.R. D. is supported by an STFC Ernest Rutherford Fellowship: ST/W003449/1. J.M.J. acknowledges support from the Jet Propulsion Laboratory, California Institute of Technology, under a contract with the National Aeronautics and Space Administration (contract 80NM0018D0004). C.P. acknowledges

internal support from the University of

Oregon.

Belcher, J. W., Lazarus, A. J., McNutt, R. L., Jr., & Gordon, G. S., Jr. (1993). Solar wind conditions in the outer heliosphere and the distance to the termination shock. *Journal of Geophysical Research*, 98(A9), 15177–15183. https://doi.org/10.1029/93JA01178

Bodewits, D., Christian, D. J., Torney, M., Dryer, M., Lisse, C. M., Dennerl, K., et al. (2007). Spectral analysis of the chandra comet survey. Astronomy & Astrophysics, 469(3), 1183–1195. https://doi.org/10.1051/0004-6361:20077410

Bridge, H. S., Belcher, J. W., Coppi, B., Lazarus, A. J., McNutt, R. L., Olbert, S., et al. (1986). Plasma observations near Uranus: Initial results from voyager 2. Science, 233(4759), 89–93. https://doi.org/10.1126/science.233.4759.89

from voyager 2. Science, 233(4759), 89–93. https://doi.org/10.1126/science.233.4759.89
Cao, X., & Paty, C. (2017). Diurnal and seasonal variability of uranus's magnetosphere. Journal of Geophysical Research: Space Physics, 122(6),

6318-6331. https://doi.org/10.1002/2017JA024063
Cao, X., & Paty, C. (2021). Asymmetric structure of uranus' magnetopause controlled by IMF and planetary rotation. *Geophysical Research*

Cao, X., & Paty, C. S. (2014). A seasonal study of uranus' magnetosphere. Agu fall meeting abstracts, 2014, SM51E-4283.

Carter, J. A., & Sembay, S. (2008). Identifying xmm-newton observations affected by solar wind charge exchange. Part I. Astronomy & Astrophysics, 489(2), 837–848. https://doi.org/10.1051/0004-6361:200809997

Carter, J. A., Sembay, S., & Read, A. M. (2010). A high charge state coronal mass ejection seen through solar wind charge exchange emission as detected by xmm-newton. *Monthly Notices of the Royal Astronomical Society*, 402(2), 867–878. https://doi.org/10.1111/j.1365-2966.2009. 15985.x

Carter, J. A., Sembay, S., & Read, A. M. (2011). Identifying xmm-newton observations affected by solar wind charge exchange – Part ii. Astronomy & Astrophysics, 527, A115. https://doi.org/10.1051/0004-6361/201015817

NAYLOR ET AL. 15 of 17



- Cheng, A. F. (1987). Proton and oxygen plasmas at Uranus. Journal of Geophysical Research, 92(A13), 15309–15314. https://doi.org/10.1029/ JA092iA13p15309
- Collier, M. R., Snowden, S. L., Sarantos, M., Benna, M., Carter, J. A., Cravens, T. E., et al. (2014). On lunar exospheric column densities and solar wind access beyond the terminator from rosat soft x-ray observations of solar wind charge exchange. *Journal of Geophysical Research: Planets*. 119(7), 1459–1478. https://doi.org/10.1002/2014JE004628
- Connor, H. K., Sibeck, D. G., Collier, M. R., Baliukin, I. I., Branduardi-Raymont, G., Brandt, P. C., et al. (2021). Soft x-ray and ena imaging of the earth's dayside magnetosphere. *Journal of Geophysical Research: Space Physics*, 126(3), e2020JA028816. https://doi.org/10.1029/2020JA028816
- Cravens, T. E. (1997). Comet hyakutake x-ray source: Charge transfer of solar wind heavy ions. *Geophysical Research Letters*, 24(1), 105–108. https://doi.org/10.1029/96GL03780
- Cravens, T. E. (2000). Heliospheric x-ray emission associated with charge transfer of the solar wind with interstellar neutrals. *The Astrophysical Journal*, 532(2), L153–L156. https://doi.org/10.1086/312574
- Cravens, T. E., Howell, E., Waite, J. H., Jr., & Gladstone, G. R. (1995). Auroral oxygen precipitation at Jupiter. *Journal of Geophysical Research*, 100(A9), 17153–17161. https://doi.org/10.1029/95JA00970
- Cravens, T. E., Robertson, I. P., & Snowden, S. L. (2001). Temporal variations of geocoronal and heliospheric x-ray emission associated with the solar wind interaction with neutrals. *Journal of Geophysical Research*, 106(A11), 24883–24892. https://doi.org/10.1029/2000JA000461
- Cravens, T. E., Waite, J. H., Gombosi, T. I., Lugaz, N., Gladstone, G. R., Mauk, B. H., & MacDowall, R. J. (2003). Implications of Jovian x-ray emission for magnetosphere-ionosphere coupling. *Journal of Geophysical Research*, 108(A12), 1465. https://doi.org/10.1029/2003JA010050
- Dennerl, K. (2008). X-rays from Venus observed with chandra. *Planetary and Space Science*, 56(10), 1414–1423. (Ground-based and Venus Express Coordinated Campaign). https://doi.org/10.1016/j.pss.2008.03.008
- Dunn, W. R., Branduardi-Raymont, G., Carter-Cortez, V., Campbell, A., Elsner, R., Ness, J.-U., et al. (2020). Jupiter's x-ray emission during the 2007 solar minimum. *Journal of Geophysical Research: Space Physics*, 125(6), e2019JA027219. https://doi.org/10.1029/2019JA027219
- Dunn, W. R., Ness, J.-U., Lamy, L., Tremblay, G. R., Branduardi-Raymont, G., Snios, B., et al. (2021). A low signal detection of x-rays from Uranus. *Journal of Geophysical Research: Space Physics*, 126(4), e2020JA028739. https://doi.org/10.1029/2020JA028739
- Dunn, W. R., Weigt, D. M., Grodent, D., Yao, Z. H., May, D., Feigelman, K., et al. (2022). Jupiter's x-ray and uv dark polar region. *Geophysical Research Letters*, 49(11), e2021GL097390. https://doi.org/10.1029/2021GL097390
- Eviatar, A., & Richardson, J. D. (1986). Predicted satellite plasma Tori in the magnetosphere of Uranus. apjl, 300, L99. https://doi.org/10.1086/184611
- Farris, M. H., Petrinec, S. M., & Russell, C. T. (1991). The thickness of the magnetosheath: Constraints on the polytropic index. *Geophysical Research Letters*, 18(10), 1821–1824. https://doi.org/10.1029/91GL02090
- Farris, M. H., & Russell, C. T. (1994). Determining the standoff distance of the bow shock: Mach number dependence and use of models. *Journal of Geophysical Research*, 99(A9), 17681–17689. https://doi.org/10.1029/94JA01020
- Fraser, G., Carpenter, J., Rothery, D., Pearson, J., Martindale, A., Huovelin, J., et al. (2010). The Mercury imaging x-ray spectrometer (mixs) on bepicolombo. *Planetary and Space Science*, 58(1), 79–95. (ComprehensiveScienceInvestigationsofMercury: The scientific goals of the joint ESA/JAXA mission BepiColombo). https://doi.org/10.1016/j.pss.2009.05.004
- Galeazzi, M., Chiao, M., Collier, M. R., Cravens, T., Koutroumpa, D., Kuntz, K. D., et al. (2011). Dxl: A sounding rocket mission for the study of solar wind charge exchange and local hot bubble x-ray emission. *Experimental Astronomy*, 32(2), 83–99. https://doi.org/10.1007/s10686-011-9249-v
- Galeazzi, M., Collier, M., Cravens, T., Koutroumpa, D., Kuntz, K., Lepri, S., et al. (2012). Solar wind charge exchange and local hot bubble x-ray emission with the dxl sounding rocket experiment. Astronomische Nachrichten, 333(4), 383–387. https://doi.org/10.1002/asna.201211665
- Gershman, D. J., & DiBraccio, G. A. (2024). Quantifying external energy inputs for giant planet magnetospheres. *Geophysical Research Letters*, 51(15), e2024GL109660. https://doi.org/10.1029/2024GL109660
- Giacconi, R., Gursky, H., Paolini, F. R., & Rossi, B. B. (1962). Evidence for x rays from sources outside the solar system. *Physical Review Letters*, 9(11), 439–443. https://doi.org/10.1103/PhysRevLett.9.439
- Herbert, F., Sandel, B. R., Yelle, R. V., Holberg, J. B., Broadfoot, A. L., Shemansky, D. E., et al. (1987). The upper atmosphere of Uranus: Euv occultations observed by voyager 2. *Journal of Geophysical Research*, 92(A13), 15093–15109. https://doi.org/10.1029/JA092iA13p15093
- Jasinski, J. M., Cochrane, C. J., Jia, X., Dunn, W. R., Roussos, E., Nordheim, T. A., et al. (2024). The anomalous state of Uranus's magnetosphere during the voyager 2 flyby. *Nature Astronomy*, 9(1), 66–74. https://doi.org/10.1038/s41550-024-02389-3
- Jasinski, J. M., Murphy, N., Jia, X., & Slavin, J. A. (2022). Neptune's pole-on magnetosphere: Dayside reconnection observations by voyager 2. The Planetary Science Journal, 3(4), 76. https://doi.org/10.3847/PSJ/ac5967
- Koutroumpa, D., Lallement, R., Kharchenko, V., Dalgarno, A., Pepino, R., Izmodenov, V., & Quémerais, E. (2006). Charge-transfer induced euv and soft x-ray emissions in the heliosphere. *Astronomy & Astrophysics*, 460(1), 289–300. https://doi.org/10.1051/0004-6361:20065250
- Kuntz, K. D., & Snowden, S. L. (2000). Deconstructing the spectrum of the soft x-ray background. The Astrophysical Journal, 543(1), 195–215. https://doi.org/10.1086/317071
- Leppard, F., Patrick, A., Ray, L., Dunn, W. R., Smith, H. T., Yao, Z., et al. (2025). Estimating solar wind charge exchange generated soft x-rays in the Jovian magnetosheath. *Journal of Geophysical Research: Space Physics*, 130(7), e2024JA033415. https://doi.org/10.1029/2024JA033415
- Liang, G. Y., Zhu, X. L., Wei, H. G., Yuan, D. W., Zhong, J. Y., Wu, Y., et al. (2021). Charge-exchange soft x-ray emission of highly charged ions with inclusion of multiple-electron capture. *Monthly Notices of the Royal Astronomical Society*, 508(2), 2194–2203. https://doi.org/10.1093/mnras/stab2537
- Lisse, C. M., Dennerl, K., Englhauser, J., Harden, M., Marshall, F. E., Mumma, M. J., et al. (1996). Discovery of x-ray and extreme ultraviolet emission from comet c/hyakutake 1996 b2. Science, 274(5285), 205–209. https://doi.org/10.1126/science.274.5285.205
- Metzger, A. E., Gilman, D. A., Luthey, J. L., Hurley, K. C., Schnopper, H. W., Seward, F. D., & Sullivan, J. D. (1983). The detection of x rays from Jupiter. *Journal of Geophysical Research*, 88(A10), 7731–7741. https://doi.org/10.1029/JA088iA10p07731
- National Academies of Sciences, Engineering, and Medicine. (2023). Origins, worlds, and life: A decadal strategy for planetary science and astrobiology 2023-2032. Washington, DC: The National Academies Press. https://doi.org/10.17226/26522
- Naylor, D., Ray, L. C., Dunn, W. R., Jasinski, J. M., & Paty, C. (2025). Data: Estimating soft x-ray emission from uranus's magnetosheath. Lancaster University. https://doi.org/10.17635/lancaster/researchdata/711
- Ness, N. F., Acuña, M. H., Behannon, K. W., Burlaga, L. F., Connerney, J. E. P., Lepping, R. P., & Neubauer, F. M. (1986). Magnetic fields at Uranus. *Science*, 233(4759), 85–89. https://doi.org/10.1126/science.233.4759.85
- Paty, C., Arridge, C. S., Cohen, I. J., DiBraccio, G. A., Ebert, R. W., & Rymer, A. M. (2020). Ice giant magnetospheres. *Philosophical Transactions of the Royal Society A: Mathematical, Physical and Engineering Sciences*, 378(2187), 20190480. https://doi.org/10.1098/rsta.2019.0480

NAYLOR ET AL. 16 of 17



- Petrinec, S. M., & Russell, C. T. (1997). Hydrodynamic and mhd equations across the bow shock and along the surfaces of planetary obstacles. Space Science Reviews, 79(3–4), 757–791. https://doi.org/10.1023/a:1004938724300
- Prolss, G. W. (2010). Physics of the earth's space environment: An introduction. Berlin: Springer-Verlag.
- Richardson, J. D., Zhang, M., Belcher, J. W., & Siscoe, G. L. (1990). Plasma fluctuations in the magnetosheath downstream from Uranus. *Journal of Geophysical Research*, 95(A5), 6413–6421. https://doi.org/10.1029/JA095iA05p06413
- Schwadron, N. A., & Cravens, T. E. (2000). Implications of solar wind composition for cometary x-rays. *The Astrophysical Journal*, 544(1), 558–566. https://doi.org/10.1086/317176
- Sembay, S., Alme, A. L., Agnolon, D., Arnold, T., Beardmore, A., Margeli, A. B. B., et al. (2024). The soft x-ray imager (sxi) on the smile mission. Earth and Planetary Physics, 8(1), 5–14. https://doi.org/10.26464/epp2023067
- Shue, J.-H., Chao, J. K., Fu, H. C., Russell, C. T., Song, P., Khurana, K. K., & Singer, H. J. (1997). A new functional form to study the solar wind control of the magnetopause size and shape. *Journal of Geophysical Research*, 102(A5), 9497–9511. https://doi.org/10.1029/97JA00196
- Sibeck, D. G., Allen, R., Aryan, H., Bodewits, D., Brandt, P., Branduardi-Raymont, G., et al. (2018). Imaging plasma density structures in the soft X-Rays generated by solar wind charge exchange with neutrals. *Space Science Reviews*, 214(4), 79. https://doi.org/10.1007/s11214-018-0504-7
- Smith, R. K., Foster, A., & Brickhouse, N. (2012). Approximating the x-ray spectrum emitted from astrophysical charge exchange. *Astronomische Nachrichten*, 333(4), 301–304. https://doi.org/10.1002/asna.201211673
- Smith, R. K., Foster, A. R., Edgar, R. J., & Brickhouse, N. S. (2014). Resolving the origin of the diffuse soft x-ray background. *The Astrophysical Journal*, 787(1), 77. https://doi.org/10.1088/0004-637X/787/1/77
- Snowden, S. L., Collier, M. R., & Kuntz, K. D. (2004). Xmm-newton observation of solar wind charge exchange emission. *The Astrophysical Journal*, 610(2), 1182–1190. https://doi.org/10.1086/421841
- Snowden, S. L., Cox, D. P., McCammon, D., & Sanders, W. T. (1990). A model for the distribution of material generating the soft X-Ray background. *The Astrophysical Journal*, 354, 211. https://doi.org/10.1086/168680
- Snowden, S. L., Egger, R., Freyberg, M. J., McCammon, D., Plucinsky, P. P., Sanders, W. T., et al. (1997). Rosat survey diffuse x-ray background maps, ii. *The Astrophysical Journal*, 485(1), 125–135. https://doi.org/10.1086/304399
- Spreiter, J. R., Summers, A. L., & Alksne, A. Y. (1966). Hydromagnetic flow around the magnetosphere. *Planetary and Space Science*, 14(3), 223–253. https://doi.org/10.1016/0032-0633(66)90124-3
- Stone, E. C., & Miner, E. D. (1986). The voyager 2 encounter with the Uranian system. *Science*, 233(4759), 39–43. https://doi.org/10.1126/science.233.4759.39
- Thomas, N. E., Carter, J. A., Chiao, M. P., Chornay, D. J., Collado-Vega, Y. M., Collier, M. R., et al. (2013). The DXL and STORM sounding rocket mission. In O. H. Siegmund (Ed.), *Uv*, *x-ray*, and gamma-ray space instrumentation for astronomy xviii (Vol. 8859, p. 88590Z). SPIE. https://doi.org/10.1117/12.2024438
- Tóth, G., Kovács, D., Hansen, K. C., & Gombosi, T. I. (2004). Three-dimensional mhd simulations of the magnetosphere of uranus. *Journal of Geophysical Research*, 109(A11), A11210. https://doi.org/10.1029/2004JA010406
- Voigt, G. H., Behannon, K. W., & Ness, N. F. (1987). Magnetic field and current structures in the magnetosphere of Uranus. *Journal of Geophysical Research*, 92(A13), 15337–15346. https://doi.org/10.1029/JA092iA13p15337
- Voitcu, G., & Echim, M. (2024). Numerical simulation of soft X-ray signature of high-speed magnetosheath jets. 45th cospar scientific assembly, 45, 1293.
- von Steiger, R., Schwadron, N. A., Fisk, L. A., Geiss, J., Gloeckler, G., Hefti, S., et al. (2000). Composition of quasi-stationary solar wind flows from ulysses/solar wind ion composition spectrometer. *Journal of Geophysical Research*, 105(A12), 27217–27238. https://doi.org/10.1029/1999IA000358
- Walsh, B. M., Kuntz, K. D., Busk, S., Cameron, T., Chornay, D., Chuchra, A., et al. (2024). The lunar environment heliophysics X-ray imager (LEXI) mission. Space Science Reviews, 220(4), 37. https://doi.org/10.1007/s11214-024-01063-4
- Wertz, J. R., & Larson, J. R. (1999). Space mission analysis and design (3rd ed.). Torrance. Calif: Microcosm Press.
- Whittaker, I. C., & Sembay, S. (2016). A comparison of empirical and experimental o7+, o8+, and o/h values, with applications to terrestrial solar wind charge exchange. Geophysical Research Letters, 43(14), 7328–7337. https://doi.org/10.1002/2016GL069914
- Whittaker, I. C., Sembay, S., Carter, J. A., Read, A. M., Milan, S. E., & Palmroth, M. (2016). Modeling the magnetospheric x-ray emission from solar wind charge exchange with verification from xmm-newton observations. *Journal of Geophysical Research: Space Physics*, 121(5), 4158–4179. https://doi.org/10.1002/2015JA022292
- Wibisono, A. D., Branduardi-Raymont, G., Dunn, W. R., Coates, A. J., Weigt, D. M., Jackman, C. M., et al. (2020). Temporal and spectral studies by xmm-newton of jupiter's x-ray auroras during a compression event. *Journal of Geophysical Research: Space Physics*, 125(5), e2019JA027676. https://doi.org/10.1029/2019JA027676
- Xu, Q., Koutroumpa, D., Modolo, R., Sun, T., Connor, H., Sembay, S., & Tkachenko, Y. (2024). Modeling soft x-ray emissions at the dayside magnetopause. *Journal of Geophysical Research: Space Physics*, 129(8), e2024JA032687. https://doi.org/10.1029/2024JA032687

NAYLOR ET AL. 17 of 17